Langmuir

Article

pubs.acs.org/Langmuir

Morphology Modulating the Wettability of a Diamond Film

Shibing Tian,[†] Weijie Sun,[†] Zhaosheng Hu,[†] Baogang Quan,[†] Xiaoxiang Xia,[†] Yunlong Li,[†] Dong Han,[‡] Junjie Li,*[,†] and Changzhi Gu*[,†]

[†]Beijing National Laboratory for Condensed Matter Physics, Institute of Physics, Chinese Academy of Sciences, Beijing 100190, China

[‡]National Centre for NanoScience and Technology, Beijing 100190, China

ABSTRACT: Control of the wetting property of diamond surface has been a challenge because of its maximal hardness and good chemical inertness. In this work, the micro/nanoarray structures etched into diamond film surfaces by a maskless plasma method are shown to fix a surface's wettability characteristics, and this means that the change in morphology is able to modulate the wettability of a diamond film from weakly hydrophilic to either superhydrophilic or superhydrophobic. It can be seen that the etched diamond surface with a mushroom-shaped array is superhydrophobic following the Cassie mode, whereas the etched surface with nanocone arrays is superhydrophilic in accordance with the hemiwicking mechnism. In addition, the difference in cone densities of superhydrophilic nanocone surfaces has a significant effect on water spreading, which is mainly derived from different driving forces. This low-cost and convenient means of altering the wetting properties of diamond surfaces can be further applied to underlying wetting phenomena and expand the applications of diamond in various fields.

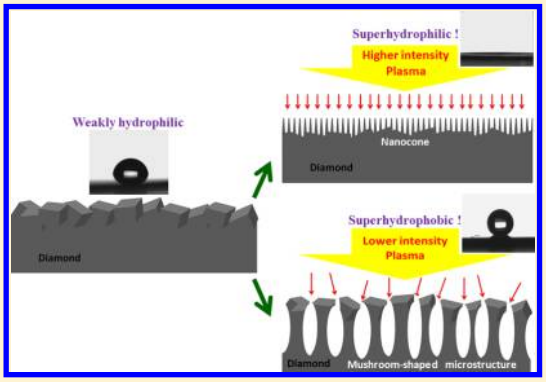

1. INTRODUCTION

The wetting behavior of diamond surfaces has been a subject of great concern in recent years because of the wetting behavior's critical role in biofunctional applications, and thus conditioning a diamond surface to a particular wettable behavior in the range between superhydrophilic and superhydrophobic has become a prominent aim in recent research. However, owing to the maximal hardness and chemical inertness of diamond, it is difficult to change the wetting properties of its surface by introducing either roughness or chemical decoration, though these are the main methods that have been attempted.

Control of the wetting property of a diamond surface has been a key issue in its biosensing and biofunctionalization applications ever since this material was discovered to be perfectly biocompatible.[1−5] Many efforts have been made to modulate the superwettability of the diamond surface, overcoming its initial weak hydrophilicity to achieve either superhydrophilicity (e.g., apparent contact angle (CA) almost 0°)[6] or superhydrophobicity (e.g., apparent CA above 150° and low CA hysteresis)[7] for various objectives.[8−24] Most attempts follow one of two general strategies. One strategy is to change the surface energy chemically, e.g., in hydrogen-terminated diamond, oxidized diamond,[9,10] perfluorooctyl functional diamond,[18] and ion implanted diamond,[19] which certainly can improve the wetting properties of the diamond surface to some extent, if only for a short time. However, such chemical methods hardly satisfy common application requirements for sustained and long-term functioning of the thin diamond film surface, especially under the influence of fluid media in biosensor applications.[14] The other common strategy is to rough up the diamond surface, usually by plasma etching. In this way, diamond can be tuned to be superhydrophilic when micro/nanoconical or needlelike arrays are formed on the diamond surface by maskless technology[12] or superhydrophobic when microscale nail-shaped structures are fabricated with an inverse template[15] or lithography,[16] though such processing is complex.[17] It is worth noting that roughness-induced superwettability is more stable than the superwettability induced by chemical modifications. In particular, maskless etching appears to be somewhat more practical than the other methods commonly discussed because of its low cost and convenience. Nevertheless, to the best of our knowledge, no one has reported making a diamond surface superhydrophobic by means of maskless etching. Low-cost, convenient fabrication of a robust superhydrophobic diamond surface is still a real challenge. In addition to superhydrophobicity, superhydrophilicity has been a hot research subject for some time in surface science and engineering. Such surfaces have their own potentially useful features such as ultrafast drying, antifogging, and self-cleaning.[25,26] Applications in heat transfer[27] and biomolecular immobilization[28] have also been reported. Generally, the superhydrophilicity of a surface is defined by the fact that the apparent contact angle is zero, on which the water can easily invade the roughness and spreads completely.[29,30] And the temporal evolution of water droplet's shape on a superhydrophilic surface has drawn much scientific

Received: June 10, 2014
Revised: September 20, 2014
Published: October 3, 2014

   dx.doi.org/10.1021/la5022643 | *Langmuir* 2014, 30, 12647−12653

interest, especially regarding how the morphology of microstructures on the surface affect such a process.[2,14,19]

In this work, we give the first report of a simple way to fabricate a superwettable surface on a diamond film using maskless plasma etching. In this process, the plasma density and intensity are controlled to reshape the micro/nanoscale morphology of the diamond film's surface. In one interesting result of our plasma etching experiments, a superhydrophobic diamond surface with mushroom-shaped microstructures was formed via low-intensity plasma etching. In addition, by high-intensity plasma etching, a series of superhydrophilic diamond film samples were etched, leaving nanocone arrays of different densities and cone shapes on their surfaces. The nanocones' dimensions and their array density both affect the spreading process of a water droplet on such a superhydrophilic diamond surface, as will be discussed here in detail. Thus, we provide an all-purpose maskless plasma etching method for fabricating a range of diamond surface morphologies that fix the surface's wettability behavior anywhere in the range from superhydrophilic to superhydrophobic. The mechanism by which these morphologies affect the wettability is analyzed in detail. In addition, in the superhydrophilic samples, the spreading velocity of a water droplet on densely arrayed, sharp nanocones is about 2 orders of magnitude faster than on less dense, blunter nanocones, and that effect should be considered when analyzing hydrophilic wetting in general.

2. EXPERIMENTAL SECTION

Fabrication of the Micro/Nanostructure in the Diamond Film Surface. In a double-bias-assisted HFCVD system shown in Figure 1, a mixed gas of CH_4 and H_2 with a CH_4 concentration of

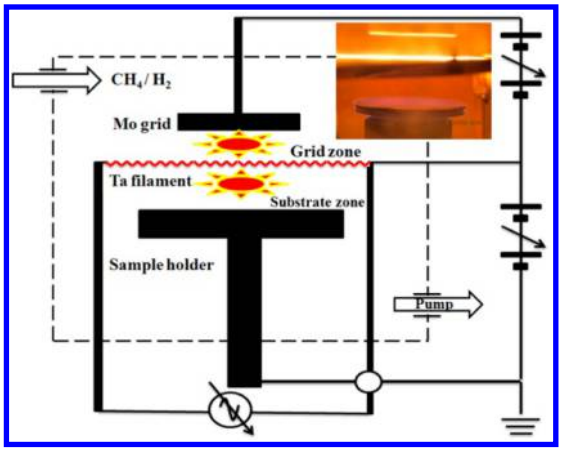

Figure 1. Schematic of the apparatus used to modulate the morphology of the diamond surface. The inset is a real plasma photograph of the grid-electrode region and substrate region.

2.0% was introduced into the chamber; the working pressure was 4000 Pa, and the tantalum filament was heated to about 2000 °C. A 3 cm molybdenum grid electrode was constructed 1 cm above the planar tantalum filament, and a positive bias relative to the filament was applied to the grid; then a negative bias was applied between the sample and filament, which were about 0.9 cm apart. For the fabrication of nanocone structures, a high grid bias of 30 V with a bias current of 30−70 A and a relatively high sample bias of 100 V with a bias current above 150 mA were applied for 5 min. Figure 6a−c corresponds to diamond nanocone arrays with different densities, which are fabricated by using the same high grid bias of 30 V with different bias currents of 70, 50, and 30 A and applying a high sample bias of 100 V with a consistent bias current of 150 mA. In addition, the mushroom microstructures are formed under a low grid bias of 5 V with a bias current above 5 A and a low sample bias of 11 V with a bias current of 20 mA for 2 h. During the etching process, the substrate temperature is kept at about 900 °C. In addition, the polished diamond films are prepared by mechanical polishing of the original diamond film, which are used for comparison.

Characterization and Wetting-Property Measurements. The morphology, structure, and chemical bond state of the samples were characterized by scanning electron microscopy (SEM) images and Raman spectra. The static contact angles (CAs) and the spreading behavior of water droplets loaded onto these etched diamond structures were measured in real time using a KRUSS DSA contact angle goniometer.

3. RESULTS AND DISCUSSION

Fabrication and Characterization. Morphology-based conditioning of the wettability of a diamond film surface is accomplished by selective plasma etching using a specially made double-bias-assisted hot filament chemical vapor deposition (HFCVD) system, shown in Figure 1. (For details and conditions, see the Experimental Section.) In this etching system, ordinary CH_4 and H_2 are mixed as the etching gas, but the system has a dual-bias-assisted configuration, unlike common HFCVD equipment. Two plasma regions are generated by the dual bias in this etching system: a grid-electrode region and a sample region, as shown in Figure 1. In the grid-electrode region, the plasma can be easily generated by hot electrons emitted from the filament and accelerated by a positive bias. The ions and reactive species in this plasma region can be induced by a negative bias to relocate in the sample region so that plasma can be generated in the sample region and etch a new morphology in the diamond surface for the purpose of tuning the material's wettability. When such a method is used, the plasma density can be readily controlled by the grid-electrode's bias while the plasma intensity for etching the diamond can also be easily adjusted by the sample's bias.[31,32]

Figure 2a shows SEM images of an unetched polycrystalline diamond film with a rough surface and a large grain size. After a controlled etching process, two typical micromorphologies with respective micro/nanostructures on diamond film surfaces are achieved, as shown in Figure 2b,c. Figure 2b shows a high-density array of nanocone diamond structures distributed uniformly over the diamond surface, which is a very popular nanostructure with multiple functional properties. Furthermore, novel mushroomlike microstructures of diamond in forestlike arrays were also fabricated on the surfaces of diamond films, with each mushroom having a large cap from 10 μm to several tens of micrometers in size. The great difference between these two diamond structures is attributable to the plasma intensity during the etching process. Figure 2d shows Raman spectra of the diamond surface before and after plasma etching, indicating that the etching process has not damaged the intrinsic properties of the diamond film. A characteristic peak of diamond at 1332 cm^{-1} is weakened after the etching process, and two new peaks appear at about 1080 and 1610 cm^{-1}, assigned to sp^2-rich amorphous carbon. The above Raman results indicate that the surface chemical state of the unetched diamond film may be different from that of the etched diamond film, but the surface chemical state of the as-etched mushroom-shaped array surface should be similar to that of the as-ethced nanocone array surface as a result of the same etching process for an original diamond film. Here we mainly focus on the

dx.doi.org/10.1021/la5022643 | Langmuir 2014, 30, 12647−12653

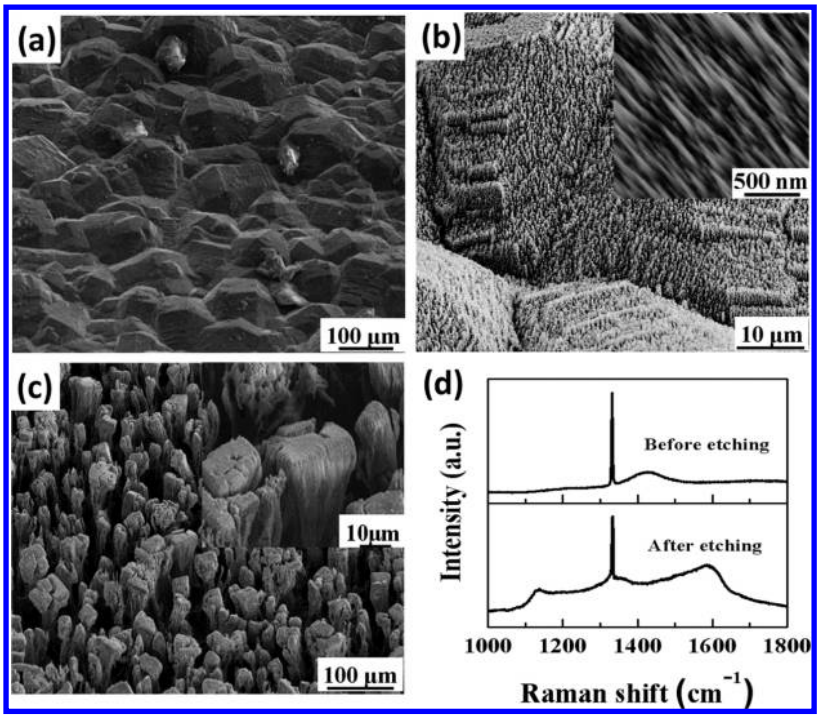

Figure 2. SEM images of the diamond surface: (a) the polycrystalline diamond surface used as a substrate, (b) the nanocone diamond structures, with an inset showing the details of the nanocones, and (c) the mushroom-shaped structures, with an inset showing the details of mushroom-shaped structures. (d) Raman spectra of the diamond film substrate before and after plasma etching.

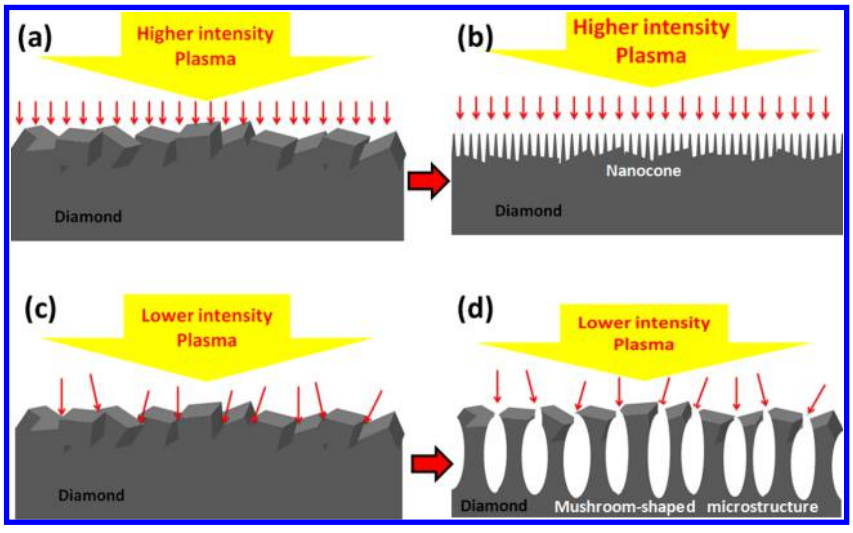

Figure 3. Schematic of the formation of diamond structures: (a) homogeneous etching of the polycrystalline diamond surface; (b) formation of nanocone diamond array structures; (c) selective etching of the polycrystalline diamond surface; and (d) formation of the arrayed mushroom-shaped diamond structures.

wettability modulation by physical morphology for similar surface chemical states.

The fabrication of these two kinds of diamond structures is achieved by control of the plasma intensity and energy distribution. Figure 3 shows a schematic for fabricating the two structures. Upon applying a high grid bias of 30 V with a bias current above 30 A and a relatively high sample bias of 100 V with a bias current above 150 mA, there is high-density plasma in the grid region and high-intensity plasma in the sample zone. In etching-plasma devices configured this way, the ions and reactive species can etch the diamond surface homogeneously. As a result, during 5 min of etching, the nanocone array structure forms uniformly on the diamond surface, as schematically shown in Figure 3a,b. However, by applying a low grid bias of 5 V with current above 5 A and a low sample bias of 11 V with a current of 20 mA, under the same experimental conditions, the intensity of the downward plasma flow is not able to break the carbon sp^3 bonds of the diamond surface but it can damage the interfaces of diamond crystal grains where carbon sp^2 bonds are plentiful.[15−18,33] And thus, this low-intensity plasma etching selectively etches polycrystalline diamond surfaces. Consequently, after keeping up such a selective etching process for about 2 to 3 h, we found that a roughly uniform array of mushroom-shaped microstructures forms on the diamond surface, as displayed schematically in Figure 3c,d. So the difference between the grain boundary

dx.doi.org/10.1021/la5022643 | *Langmuir* 2014, 30, 12647−12653

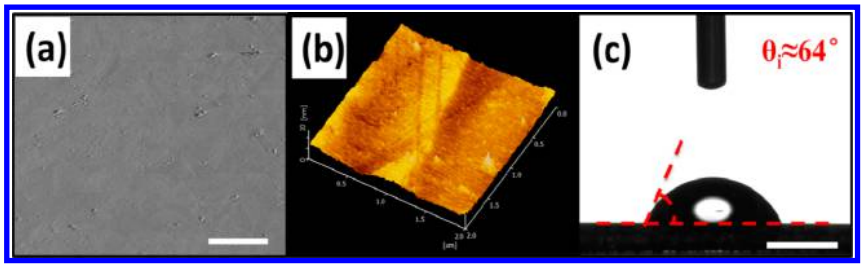

Figure 4. SEM and AFM images of the polished diamond surface and its wetting property: (a) SEM image with a scale bar of 5 μm, (b) AFM image, and (c) static CA of water on the polished diamond surface with a scale bar of 1 mm.

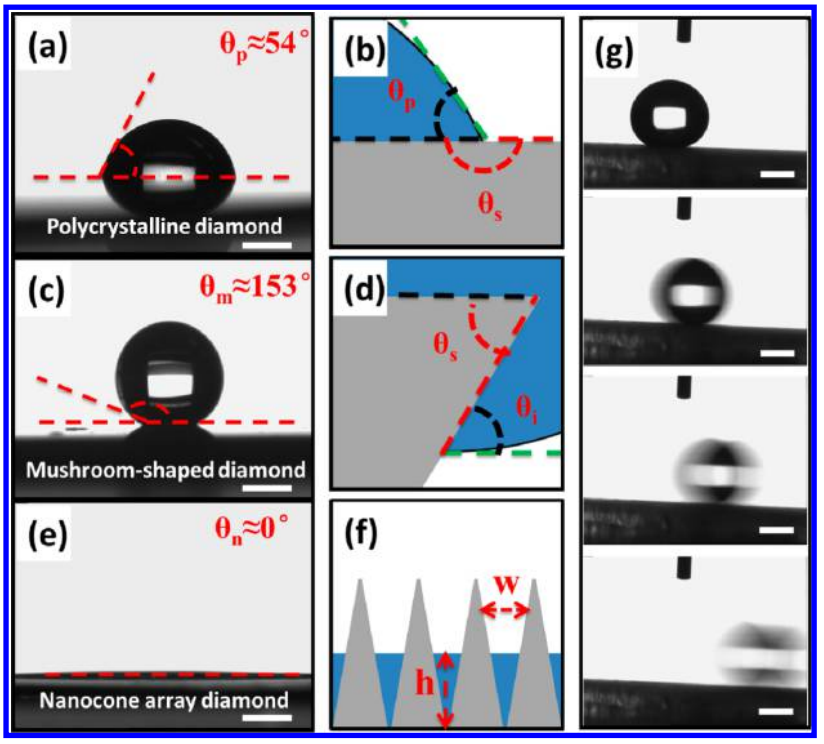

Figure 5. Static CAs of water on diamond surfaces and schematic of the wetting mechanism: (a, b) for polycrystalline diamond, (c, d) for mushroom-shaped structures, and (e, f) for a nanocone array. (g) Rolling process of a water droplet on mushroom-shaped structures. The scale bar is 1 mm.

energy and surface energy, together with successful control of the density and intensity of the plasma in our apparatus, provided a method for selectively etching the diamond to form various micro/nanostructures.

Wettability and Mechanism. Before we discuss the wetting property of a modified diamond film, it is necessary to know the wetting property of a smooth diamond surface. Figure 4 shows the morphology and wetting property of the polished polycrystalline diamond film, similar to a natural diamond surface. Though some defects coming from the CVD growth of diamond, the polished diamond film still exhibits a rather smooth surface as shown in Figure 4a, demonstrated by the AFM scanning image with an rms roughness of ~0.79 nm, as shown in Figure 4b. Figure 4c gives the static CA of a water droplet of about 64° on the polished diamond surface with advancing and receding contact angles of 70 and 46°, which is close to an intrinsic CA on a natural diamond surface.

Figure 5 shows the tuned wetting property of the structured diamond surface and the schematic wetting mechanism. On the left, Figure 5a,c,e displays the static CAs of the unprocessed polycrystalline diamond surface ($\theta_p \approx 54°$), the microscale mushroom-shaped array surface ($\theta_m \approx 153°$), and nanocone array surface ($\theta_n \approx 0°$), respectively. It can be seen that the unprocessed diamond is weakly hydrophilic and that the etched surface with a mushroom-shaped array is superhydrophobic, whereas the etched surface with nanocone arrays is superhydrophilic. Thus, by using this maskless etching method, we can set the wetting property of a diamond surface at one of any number of points between superhydrophilic and superhydrophobic by determining its morphology. Besides, Figure 5g shows the process of the water droplet rolling away from the microscale mushroom-shaped array surface after sliding on the surface about 3°, indirectly demonstrating low contact angle hysteresis with advancing and receding contact angles of 159 and 145°.

Figure 5b,d,f shows the schematic of the mechanism behind such phenomena, corresponding to Figure 5a,c,e, respectively. The wetting mechanism of the unprocessed diamond surface in Figure 5b is obviously easy to understand because it is similar to the wetting state on a flat plane, but for mushroom-shaped microstructure and the nanocone structure of diamond, their

dx.doi.org/10.1021/la5022643 | Langmuir 2014, 30, 12647−12653

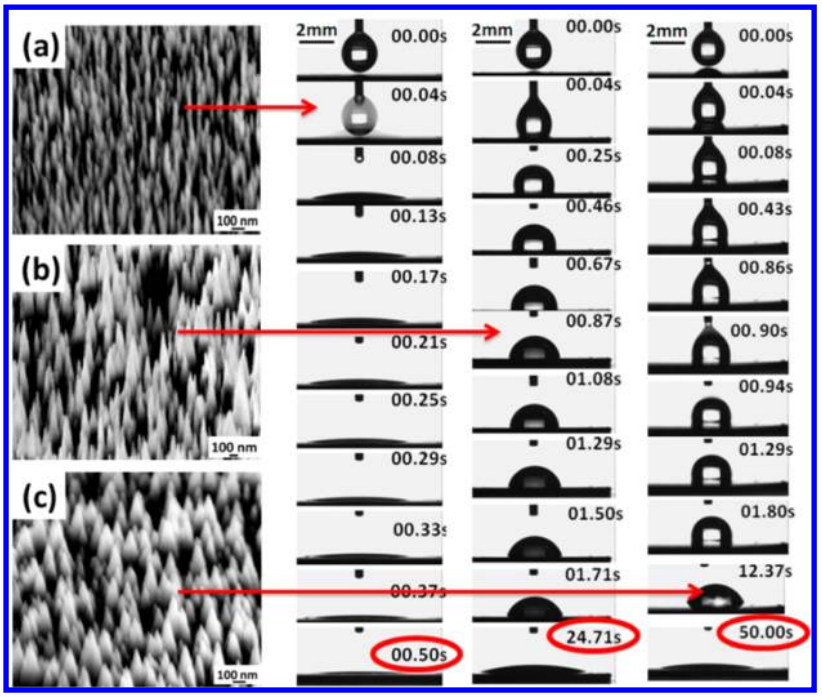

Figure 6. SEM images of diamond surfaces with different densities and profiles of nanocone arrays: (a) high density and sharp tip, (b) moderate density and moderate cone tip, (c) low density and blunt cone tip. The red arrows point to the process of water evolution on the corresponding surface.

wetting mechanisms are relatively complex in contrast to that for the unprocessed diamond surface.

First, we discuss the superhydrophobic property of the mushroom-shaped microstructure arrays on the diamond surface. As pointed out in many previous papers, the defects' (e.g., the edges of such microstructures) pining effect on the three-phase line can lead to a high energy barrier for water invading these gaps between such mushroom- or umbrella-shaped microstructures.[34−39] Figure 5d displays how the edge of a mushroom structure affects the water behavior. As the contact line reaches the edge, the contact line is pinned at the edge because of the boundary minimum of the free energy. At this moment, the apparent contact angle θ_m exceeds the intrinsic contact angle and grows with increasing droplet volume or water level. When the apparent contact angle reaches the critical angle, which depends on the solid edge angle θ_s, water extends over the edge and the contact line advances along the new surface at its intrinsic contact angle θ_i.[40,41] With a structure edge angle (θ_s) of about 50°, the possible angle θ_m of water can be in the range from θ_i to $\pi - \theta_s + \theta_i$.[42] Thus, the edges can prevent the three-phase line from moving forward and then can impede the water penetrating the gaps between micro-structures. If such a condition is satisfied, then there is an air cushion that is formed under a water droplet on such a surface; consequently, a Cassie mode or a mode mixed with a Cassie and Wenzel mode will be formed. According to the Cassie formula,[43]

$$\cos\theta = \varphi_s \cos\theta_i + \varphi_s - 1 \tag{1}$$

where θ is the apparent CA of the water on the rough surface, θ_i is the intrinsic CA of water on the smooth surface, and φ_s is the fraction of the solid in contact with the water. Here, for the diamond surface, an intrinsic CA can be obtained from the polished diamond surface as shown in Figure 4, and thus $\theta_i \approx 64°$. By eq 1, the fraction of solid in contact with the water, φ_s, is about 0.076 by using $\theta_i \approx 64°$ and $\theta_m \approx 153°$. In other words, the Cassie mode is formed on the diamond surface with the mushroom microstructure arrays. Besides, such a small fraction of solid in contact with the water can easily lead to the water droplet rolling away under an external force such as the gravity or wind flow when the inequation is satisfied as follows[36]

$$\varphi_s^{3/2}\log\left(\frac{1}{\varphi_s}\right) < R^2\kappa^2 \tag{2}$$

where is the radius of the water droplet is R and the capillary length is $\kappa^{-1} = (\gamma/\rho g)^{1/2}$ (2.7 mm for water). For our samples, R is about 1.1 mm and φ_s is about 0.076, and then the results of the left and right parts of the inequation can be calculated to be 0.023 and 0.166, respectively. Thus, the mushroom-shaped microstructure surface can satisfy eq 2, which also leads to the experimental results shown in Figure 5g. From above analysis, we can understand the mechanisms in which the diamond surface with mushroom-shaped structure arrays displays superhydrophobicity.

Second, we analyze the superhydrophilic properties derived from the cone nanostructure arrays on the diamond surface. The superhydrophilic phenomenon is usually accompanied by another important phenomenon, hemiwicking, which describes a process in which water spontaneously penetrates these gaps between such micro/nanostructures under the capillary force and the viscous resist force.[2,19,36] The criterion of hemiwicking can be written as follows:[36]

$$\frac{1-\varphi_s}{r-\varphi_s} = \cos\theta_c < \cos\theta_i = \frac{\gamma_{sv}-\gamma_{sl}}{\gamma_{lv}} \tag{3}$$

where γ_{sl}, γ_{sv}, and γ_{lv} are the solid/liquid, solid/vapor, and liquid/vapor interface energies, respectively. Parameter r stands for surface roughness. When $\theta_c > \theta_i$, hemiwicking occurs. For our superhydrophilic samples, φ_s is not uniform along the

dx.doi.org/10.1021/la5022643 | Langmuir 2014, 30, 12647−12653

normal direction of the surface because of the slide profiles of the cone structure, which is an variable and different from the situation of the micropillar arrays.[36] There are two extreme conditions when the water penetrates the cone structures with the water film thickness, as shown in Figure 5f. One is that at the bottom of these valleys, the value of φ_s is almost equal to 1 as the width of gap (w) tends to zero, and then the value of θ_c is about 90°, which is larger than the intrinsic CA, θ_i. At this time, the hemiwicking condition is satisfied and hence the water can penetrate the bottom of valleys. Inversely, another is that at the top of the cone array, the value of φ_s is almost equal to zero, and then the value of θ_c depends only on the roughness ($\cos\theta_c = 1/r$). In addition to the above two extreme conditions, the φ_s is actually a function of the water layer height from the bottom of valleys, and more details need to be discussed below.

Effect of Different Nanocone Densities on Superhydrophilic Behavior. To seek a clear and comprehensive understanding of the superhydrophilicity of the diamond nanocone surface, real-time detection methods are adopted to record the evolving behavior of water from initial contact with the surface to spreading out to present a planar surface of its own, as shown in Figure 6. Three kinds of nanocone array structures with different shapes and densities are selected as measured samples, and fabrication details are described in the Experimental Section. The as-formed nanocone array structure shown in Figure 6a has the highest density of $(2-3) \times 10^{10}$ cm^{-2}, an average apex angle of about 7°, and a height in the range of 200−300 nm. Figure 6b shows a nanocone array structure with a density of $(4-5) \times 10^{9}$ cm^{-2}, an average apex angle of about 15°, and a cone height of 200−300 nm. A lower cone density of the nanocone array of $(3-4) \times 10^{8}$ cm^{-2}, with an average apex angle of about 35° and a height of 100−200 nm, is displayed in Figure 6c.

On the right of Figure 6, the red arrow rows from the SEMs point to the real-time images of water droplet spreading on corresponding surfaces, clearly illustrating the structures' effects on the spreading velocity. With the nanocone density decreasing and the cones' apex angles increasing, the spreading velocity is tuned from high to low, the fastest spreading velocity (~6 mm/s) is 100 times greater than the slowest (~0.06 mm/s), and it is found that the increase in the spreading velocity is proportional to the increase in the nanocone density. For a similar superhydrophilic surface with a very low contact angle (<10°) after equilibrium, such a tremendous difference in the spreading velocity directly reflects the considerable different dynamic processes of water spreading out to the plain, which can be also understood by the hemiwicking mechnism.

Figure 7 displays the $\cos\theta_c - \varphi_s$ curves of the three kinds of nanocone structure surfaces with different roughness values (r), based on $\cos\theta_c = (1 - \varphi_s)/(r - \varphi_s)$ (left side of eq 3). In Figure 7, samples 1−3 stand for the nanocone structure surface of diamond with different morphologies shown in Figure 6a−c, respectively, and their roughness values (r) can be separately estimated to be 7.65, 4.04, and 2.12. In addition, the criterion of an intrinsic angle $\cos\theta_i$ is marked using a dashed line in Figure 7, and we find that the features of samples 1 and 2 are different from those of sample 3.

For samples 1 and 2, because of a greater roughness, the top layer of the cone structures can also make water penetrate. As a result, the thickness of the hemiwicking water film is equal to the height of the nanocones, and the further processing of the water droplet seems like moving on the water surface. The difference ($\delta = \cos\theta_i - \cos\theta_c$) between $\cos\theta_c$ and $\cos\theta_i$ directly reflects the change in the driving force of droplet spreading, based on the driving force equation: $F = \gamma(r - \varphi_s)(\cos\theta_i - \cos\theta_c)$.[36] In Figure 7, this difference (δ) for sample 1 is obviously larger than that for sample 2, and hence the driving force of sample 1 is higher than that for sample 2, which is the reason that the spreading velocity of sample 1 is higher than that of sample 2. These analyses agree with the experiment results shown in Figure 6a,b. Compared to samples 1 and 2, sample 3 has a lower roughness, and the top of the nanocone structures hardly affects the hemiwicking of water because the criterion $\cos\theta_c > \cos\theta_i$ is not satisfied in the case that is shown in the partial curve of sample 3 above the dashed line of $\cos\theta_i$. However, the water droplet can still be hemiwicked at the bottom of valleys but leave unwetted and dry cone tips. Finally, when water is processed on the surface of sample 3, it displays an obvious apparent CA and then the CA slowly comes to zero (Figure 6c). This can be explained by the fact that hemiwicking continues to happen around the three-phase line and the draining is from the central part of the droplet. Despite the rim of the water film in our experiment not being observed because of the antireflection of such surfaces, the behavior of the bulk water droplet is recorded, which is consistent with the previous studies.[2,19] All in all, the difference in water spreading on the superhydrophilic nanocone surfaces is mainly derived from different driving forces that lead to the hemiwicking in our experiment.

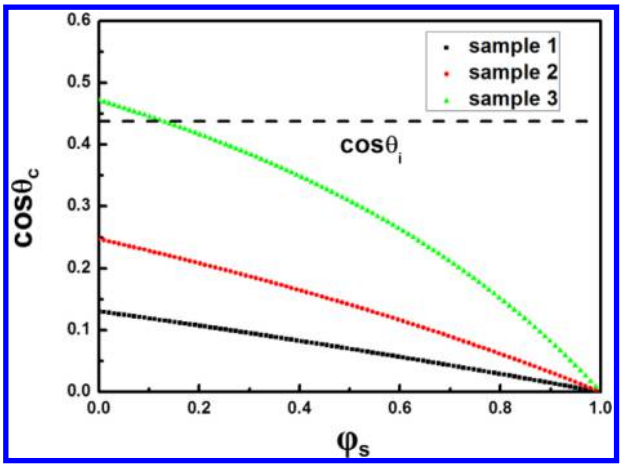

Figure 7. Change in the critical angle $\cos\theta_c$ with φ_s for three kinds of diamond nanocone surfaces with different roughness values: r = 7.75 (sample 1), r = 4.04 (sample 2), and r = 2.12 (sample 3), corresponding to different cone densities shown in Figure 6a−c, respectively. A black dashed line represents an intrinsic angle $\cos\theta_i$ of 0.438.

4. CONCLUSIONS

We used a maskless plasma etching method with a dual-bias-assisted HFCVD system to modify a series of diamond samples, resulting in samples with a range of different respective wetting behaviors−from superhydrophobic (CA ≈153°) to superhydrophilic (CA ≈ 0°). The differences are attributed to the etched surface morphologies of microstructures or nanostructures (mushroom-shaped and nanocone array structures) without any chemical modification. Moreover, these surfaces and their superwetting properties would be chemically and mechanically stable in almost any application. Upon further investigation of the superhydrophilic nanocone structure with different cone densities, we found very different spreading

dx.doi.org/10.1021/la5022643 | Langmuir 2014, 30, 12647−12653

velocities of water, spanning two orders of magnitude and depending on different surface roughness values originating from a change in nanocone density. All of this may be essential to biosensing and biomedicine applications, where a solvent's spreading velocity directly affects the final state of cells or DNA on a diamond surface. Therefore, the morphology-modulating wettability for a diamond film is important and necessary to characterize its superhydrophobic or superhydrophilic phenomena and functionalized application completely.

AUTHOR INFORMATION

Corresponding Authors

*E-mail: jjli@aphy.iphy.ac.cn.
*E-mail: czgu@aphy.iphy.ac.cn.

Notes

The authors declare no competing financial interest.

ACKNOWLEDGMENTS

We acknowledge the National Natural Science Foundation of China (grant nos. 11174362, 91023041, 91323304, 51272278, and 61390503) and the Knowledge Innovation Project of CAS (grant no. KJCX2-EW-W02).)

REFERENCES

(1) Zhuang, H.; Song, B.; Srikanth, V. V. S. S.; Jiang, X.; Schönherr, H. *J. Phys. Chem. C* **2010**, *114*, 20207−20212.
(2) Kim, S. J.; Kim, J.; Moon, M.-W.; Lee, K.-R; Kim, H.-Y. *Phys. Fluids.* **2013**, *25*, 092110.
(3) Yang, W.; Auciello, O.; Butler, J. E.; Cai, W.; Carlisle, J. A.; Gerbi, J. E.; Gruen, D. M.; Knickerbocker, T.; Lasseter, T. L.; Russell, J. N.; Smith, L. M., Jr.; Hamers, R. J. *Nat. Mater.* **2002**, *1*, 253−257.
(4) Coffinier, Y.; Szunerits, S.; Drobecq, H.; Melnyk, O.; Boukherroub, R. *Nanoscale* **2012**, *4*, 231−238.
(5) Stavis, C.; Clare, T. L.; Butler, J. E.; Radadia, A. D.; Carr, R.; Zeng, H.; King, W. P.; Carlisle, J. A.; Aksimentiev, A.; Bashir, R.; Hamers, R. J. *Proc. Natl. Acad. Sci. U.S.A.* **2011**, *108*, 983−988.
(6) Wang, R.; Hashimoto, K.; Fujishima, A.; Chikuni, M.; Kojima, E.; Kitamura, A.; Shimohigoshi, M.; Watanabe, T. *Adv. Mater.* **1998**, *10*, 135−138.
(7) Öner, D.; McCarthy, T. J. *Langmuir* **2000**, *16*, 7777−7782.
(8) Feng, X. J.; Jiang, L. *Adv. Mater.* **2006**, *18*, 3063−3078.
(9) Jiadao, W.; Darong, C.; Fengbin, L. *Adv. Tribol.* **2010**, 785−786.
(10) Yi, J. W.; Moon, M.; Ahmed, S. F.; Kim, H.; Cha, T.; Kim, H.; Kim, S.; Lee, K. *Langmuir* **2010**, *26*, 17203.
(11) Popov, C.; Vasilchina, H.; Kulisch, W.; Danneil, F.; Stüber, M.; Ulrich, S.; Welle, A.; Reithmaier, J. P. *Diamond Relat. Mater.* **2009**, *18*, 895−898.
(12) Yang, J. H. C.; Teii, K. *Diamond Relat. Mater.* **2012**, *24*, 54−58.
(13) Zhao, T.; Liu, H.; Jiang, L. *J. Nanosci. Nanotechnol.* **2010**, *10*, 7800−7803.
(14) McHale, G.; Shirtcliffe, N. J.; Aqil, S.; Perry, C. C.; Newton, M. I. *Phys. Rev. Lett.* **2004**, *93*, 036102.
(15) Sarangi, S. K.; Chattopadhyay, A.; Chattopadhyay, A. K. *Int. J. Refract. Met. Hard Mater.* **2012**, *31*, 1−13.
(16) Karlsson, M.; Forsberg, P.; Nikolajeff, F. *Langmuir* **2010**, *26*, 889−893.
(17) Zhang, W. J.; Meng, X. M.; Chan, C. Y.; Wu, Y.; Bello, I.; Lee, S. T. *Appl. Phys. Lett.* **2003**, *82*, 2622−2624.
(18) Kriele, A.; Williams, O. A.; Wolfer, M. J.; Hees, J.; Smirnov, W.; Nebel, C. E. *Chem. Phys. Lett.* **2011**, *507*, 253−259.
(19) Kim, S. J.; Moon, M.; Lee, K.; Lee, D.; Chang, Y. S.; Kim, H. *J. Fluid. Mech.* **2011**, *680*, 477−487.
(20) Marmur, A. *Langmuir* **2003**, *19*, 8343−8348.
(21) Miwa, M.; Nakajima, A.; Fujishima, A.; Hashimoto, K.; Watanabe, T. *Langmuir* **2000**, *16*, 5754−5760.
(22) Wang, S.; Zhang, Y.; Abidi, N.; Cabrales, L. *Langmuir* **2009**, *25*, 11078−11081.
(23) Li, L.; Zhang, K.; Qiu, J.; Wang, S.; Van, H. H.; Zhang, M. *Diamond Relat. Mater.* **2012**, *29*, 79−83.
(24) Su, S.; Wang, S.; Qiu, J. *Sci. Adv. Mater.* **2014**, *6*, 203−208.
(25) Chiou, N. R.; Lu, C.; Guan, J.; Lee, L. J.; Epstein, A. J. *Nat. Nanotechnol.* **2007**, *2*, 354−357.
(26) Ohdaira, T.; Nagai, H.; Kayano, S.; Kazuhito, H. *Surg. Endosc.* **2007**, *21*, 333−338.
(27) Takata, Y.; Hidaka, S.; Masuda, M.; Ito, T. *Int. J. Energy. Res.* **2003**, *27*, 111−119.
(28) Eriksson, C.; Nygren, H.; Ohlson, K. *Biomaterials* **2004**, *25*, 4759−4766.
(29) Drelich, J.; Chibowski, E.; Meng, D. D.; Terpilowski, K. *Soft Mater.* **2011**, *7*, 9804−9828.
(30) Bico, J.; Tordeux, C.; Quéré, D. *Eur. Lett.* **2001**, *55*, 214−220.
(31) Meng, L.; Zhang, J.; Zhu, X. *Thin Solid Films* **2008**, *516*, 2981−2986.
(32) Wang, Q.; Qu, S. L.; Fu, S. Y.; Liu, W. J.; Li, J. J.; Gu, C. Z. *J. Appl. Phys.* **2007**, *102*, 103714.
(33) Shiomi, H. *Jpn. J. Appl. Phys.* **1997**, *36*, 7745−7748.
(34) Tuteja, A.; Choi, W.; Ma, M.; Mabry, J. M.; Mazzella, S. A.; Rutledge, G. C.; McKinley, G. H.; Cohen, R. E. *Science* **2007**, *318*, 1618−1622.
(35) Ahuja, A.; Taylor, J. A.; Lifton, V. A.; Sidorenko, A.; Salamon, T. R.; Lobaton, E. J.; Kolodner, P.; Krupenkin, T. N. *Langmuir* **2008**, *24*, 9−14.
(36) Quéré, D. *Annu. Rev. Mater. Res.* **2008**, *38*, 71−99.
(37) Tuteja, A.; Choi, W.; Mabry, J. M.; McKinley, G. H.; Cohen, R. E. *Proc. Natl. Acad. Sci. U.S.A.* **2008**, *105*, 18200−18205.
(38) Bormashenko, E.; Whyman, G. *Langmuir* **2013**, *29*, 5515−5519.
(39) Whyman, G.; Bormashenko, E. *Langmuir* **2011**, *27*, 8171−8176.
(40) Chang, F.-M.; Hong, S.-J.; Sheng, Y.-J.; Tsao, H.-K. *J. Phys. Chem. C* **2010**, *114*, 1615−1621.
(41) Chang, F.-M.; Sheng, Y.-J.; Tsao, H.-K. *Appl. Phys. Lett.* **2009**, *95*, 204107.
(42) Oliver, J.; Huh, C.; Mason, S. *J. Colloid Interface Sci.* **1977**, *59*, 568−581.
(43) Cassie, A. B. D.; Baxter, S. *Trans. Faraday. Soc.* **1944**, *40*, 0546−0550.